Dynamical determination of the strength of cross-polarization coupling in a whispering-gallery microresonator

Limu Ke, Sreekul Raj Rajagopal, and A. T. Rosenberger*
Department of Physics, Oklahoma State University, Stillwater, Oklahoma 74078, USA

(Received 24 August 2021; revised 27 September 2021; accepted 15 November 2021; published 30 November 2021)

Cross-polarization coupling (CPC) between coresonant orthogonally polarized modes in a single whispering-gallery microresonator can lead to induced transparency effects. Depending on the CPC strength, coupled-mode-induced transparency (CMIT) or Autler-Townes splitting (ATS) can be observed. Determining the CPC strength is crucial in locating the exceptional point, where CMIT evolves into ATS and an enhancement in sensitivity to perturbations is expected. The CPC strength can be calculated theoretically based on the transverse structure of whispering-gallery modes. Experimentally, however, CPC strength has been inferred only indirectly by fitting the experimental throughput spectrum to a steady-state model. In this work, we propose and demonstrate a direct determination of the CPC strength based on the response of the throughput to a sinusoidal amplitude modulation of the input light. Our experimental results agree with numerical fitting values and are in the same range as predicted by theoretical calculations.

DOI: 10.1103/PhysRevA.104.053534

I. INTRODUCTION

Whispering-gallery mode (WGM) microresonators are advantageous for studies and applications of induced transparency effects, which can be used for signal processing and sensing [1–3]. Early observations on coupled resonators demonstrated induced transparency, induced attenuation, and Autler-Townes splitting (ATS) [4–9]. More recently, coupled-mode-induced transparency (CMIT), coupled-mode-induced attenuation (CMIA), and ATS have been observed in single WGM microresonators [10–20]; nearly all of these have involved coupling of WGMs of the same polarization but different radial orders.

Polarization effects in WGM microresonators represent a topic of increasing interest and importance [21–30]. We have previously studied CMIT resulting from cross-polarization coupling (CPC), where light of one polarization circulating in a WGM of the microresonator can be coupled into a coresonant WGM of the orthogonal polarization [21,22]. In our system, this CPC is a result of weak polarization rotation due to the optical spin-orbit interaction [21]. In this case, the input light and detected throughput are of one polarization, say TE (transverse electric). Because of CPC, the interaction with a coresonant TM (transverse magnetic) WGM produces a throughput spectrum (as the driving laser is scanned in frequency) showing cross-polarization CMIT or CMIA, observed as splitting or modification of the shape of the resonant dip. If the coupling is strong enough, CMIT turns into ATS at the exceptional point [31], where dispersion enhancement and increased sensitivity to system perturbations can be found [3,32,33]. Being able to precisely locate the exceptional point is crucial in enhancing slow light, fast light, and sensor applications of WGM microresonators, for example.

The value of the intermode coupling strength in CPC, which determines the exceptional point, can be calculated theoretically based on the transverse mode structure of WGMs if the mode orders are known [21]. Experimentally, however, the CPC strength has heretofore only been inferred indirectly by fitting the experimental throughput spectrum to a steady-state model [22].

In this paper, we propose and demonstrate a direct determination of the CPC strength based on the response of the throughput spectrum to a sinusoidal amplitude modulation of the input light [34]. First, we use a ring cavity model to analyze the dynamics of CPC and demonstrate a very nearly proportional dependence of the CPC strength on the square of the modulation frequency that gives the minimum throughput modulation amplitude on resonance (for CMIT and ATS). Then we use a hollow-bottle resonator to determine the CPC strength experimentally. This is done first by fitting the throughput spectrum to a steady-state model as before; then from the modulation frequency that gives the minimum throughput modulation amplitude, we find another estimate of the CPC strength. Our two experimental values agree with each other, and they both fall within the theoretically predicted range [21], which means we have an independent way of finding the CPC strength without the need to fit the throughput spectrum to a computer model. This gives us a better method for locating the state of the system with respect to the exceptional point and can improve sensing and other applications of WGM microresonators.

II. THEORETICAL MODEL

We use a ring cavity model as shown in Fig. 1 to study the dynamics of CPC in a microresonator. In Fig. 1, the subscripts

*atr@okstate.edu

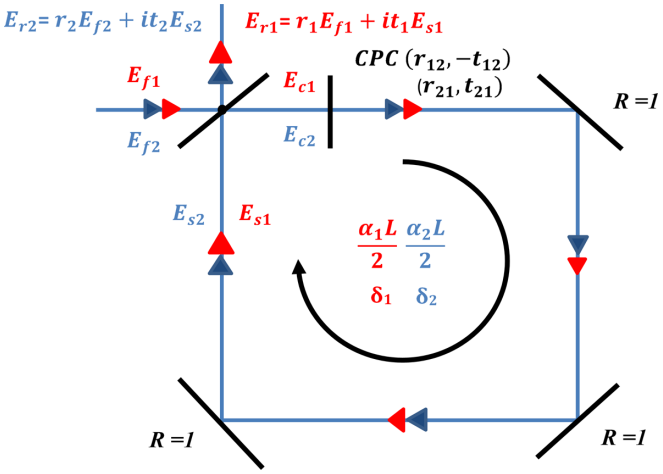

FIG. 1. Ring cavity representing tapered-fiber coupling to a microresonator with intracavity cross-polarization coupling. This figure is reproduced from Ref. [22].

1 and 2 refer to the two orthogonal polarizations. E_{fj} is the input amplitude of polarization j, and

$$E_{rj} = r_j E_{fj} + it_j E_{sj} \tag{1}$$

is the throughput amplitude of polarization j. E_{sj} is the intracavity mode amplitude just before output coupling. The input and output coupling coefficients are taken to be equal, as discussed in Ref. [22], and given by it_j, with $r_j^2 = 1-t_j^2 = 1 - T_j$.

In Fig. 1, δ_j and $\alpha_j L$ are the round-trip phase (modulo 2π) and intrinsic loss for mode j; L is the resonator circumference; the intracavity mode amplitudes just after input coupling, E_{cj}, are not used in the analysis below. Cross-polarization coupling is represented in Fig. 1 as an effective intracavity wave plate and expressed by the coefficients $-t_{12}$ and t_{21}, where $t_{12}^2 = 1-r_{12}^2$ and $t_{21}^2 = 1-r_{21}^2$ are the polarization rotation probabilities per round trip, called T_s and T_p in Ref. [21].

The intracavity mode amplitudes E_{sj} satisfy the following time evolution equations [22]:

$$\begin{aligned}\frac{d}{dt}E_{s1} &= -\gamma_1 E_{s1} - \frac{t_{12}}{\tau_{rt1}}E_{s2} + \frac{it_1}{\tau_{rt1}}E_{f1} - \frac{it_2 t_{12}}{\tau_{rt1}}E_{f2},\\ \frac{d}{dt}E_{s2} &= -\gamma_2 E_{s2} + \frac{t_{21}}{\tau_{rt2}}E_{s1} + \frac{it_2}{\tau_{rt2}}E_{f2} + \frac{it_1 t_{21}}{\tau_{rt2}}E_{f1}.\end{aligned} \tag{2}$$

With these and Eq. (1), the time evolution of the throughput amplitudes can be found. In Eq. (2), $\tau_{rtj} = n_j L/c$ is the round-trip time for mode j, where n_j is the effective refractive index of the mode, and

$$\gamma_j = \frac{T_j + \alpha_j L}{2\tau_{rtj}} - i\frac{\delta_j}{\tau_{rtj}} = \kappa_j(1 + i\theta_j), \tag{3}$$

with κ_j being the amplitude decay rate, or half the inverse of the photon lifetime in mode j, and θ_j being the offset of the resonant frequency of mode j from the input frequency in units of half the mode linewidth.

The parameters appearing in Eqs. (1)–(3) are related to experimentally measurable quantities as follows. Knowledge of the input frequency ν and measurement of the mode linewidth [full width at half maximum (FWHM) of a throughput dip] $\Delta\nu_j$ gives the quality factor Q_j of mode j and its total loss $T_j + \alpha_j L$:

$$Q_j = \frac{\nu}{\Delta\nu_j} = \frac{2\pi n_j L}{\lambda(T_j + \alpha_j L)}, \tag{4}$$

where λ is the vacuum wavelength. The coupling and intrinsic losses can be determined individually from the fractional depth M_j of a mode's resonant throughput dip and the coupling regime:

$$M_j = \frac{4x_j}{(1+x_j)^2}, \quad \text{where} \quad x_j = \frac{T_j}{\alpha_j L}. \tag{5}$$

Undercoupling and overcoupling mean $x_j < 1$ and $x_j > 1$, respectively; a given M_j can occur for two values of x_j whose product is 1, so knowledge of the coupling regime determines the values of T_j and $\alpha_j L$. The round-trip phase δ_j is related to the detuning of the input light frequency ν from the mode j resonance frequency ν_j by

$$\delta_j = \frac{2\pi n_j L}{c}(\nu - \nu_j). \tag{6}$$

In this work, only polarization 1 is input ($E_{f2} = 0$), and the CMIT effects are observed in the mode 1 throughput.

If we assume the CPC strength $T_c = t_{12}t_{21}$ is very small and both modes are resonant, Eq. (2) can be recast in the form of a second-order differential equation for E_{s1} that has the form of a damped driven oscillator. From this, the complex decay constants of the supermodes resulting from the CPC of modes 1 and 2 are found to be [22]

$$\beta_\pm = \frac{\kappa_1 + \kappa_2}{2} \pm \sqrt{\left(\frac{\kappa_1 - \kappa_2}{2}\right)^2 - \frac{T_c}{\tau_{rt1}\tau_{rt2}}}, \tag{7}$$

showing the transition from CMIT to ATS when T_c is large enough to make the radicand negative and produce frequency splitting.

Consider the case of one component where that component is the only input and is resonant and sinusoidally modulated in amplitude at frequency Ω as follows: $E_{f1} = A_{f1}e^{-i\Omega t}$, $E_{f2} = 0$. Then we have, assuming $E_{s1} = A_{s1}e^{-i\Omega t}$,

$$\frac{A_{s1}}{A_{f1}} = \frac{(\Omega + i\kappa_2)t_1/\tau_{rt1}}{\Omega_0^2 - \Omega^2 - i\Omega(\kappa_1 + \kappa_2)}, \tag{8}$$

where $\Omega_0^2 = \kappa_1\kappa_2 + T_c/\tau_{rt1}\tau_{rt2}$ is the resonance frequency of the damped driven oscillator; this leads to a way of determining the CPC coupling strength T_c. From Eqs. (8) and (1), we can find the ratio of throughput intensity to input intensity (actually, the ratio of squared modulation amplitudes) for mode 1 being driven on resonance:

$$\left|\frac{A_{r1}}{A_{f1}}\right|^2 = \frac{\left(\Omega_0^2 - \Omega^2 - T_1\kappa_2/\tau_{rt1}\right)^2 + \Omega^2(\kappa_1 + \kappa_2 - T_1/\tau_{rt1})^2}{\left(\Omega_0^2 - \Omega^2\right)^2 + \Omega^2(\kappa_1 + \kappa_2)^2}. \tag{9}$$

The ratio in Eq. (9) will be zero when both terms in the numerator vanish; for nonzero Ω, vanishing of the second term leads to the following relation to ensure vanishing of the first term,

$$\Omega_{\min}^2 = \Omega_0^2 - \kappa_2(\kappa_1 + \kappa_2) \approx \Omega_0^2 - \kappa_1\kappa_2 = \frac{T_c}{\tau_{rt}^2}, \tag{10}$$

where the two round-trip times have been taken to be equal (assuming an effective refractive index of 1.36 for each of the two WGMs [21]) and the approximation holds when the two Qs are very different, specifically when $Q_2 \gg Q_1$ (so $\kappa_2 \ll \kappa_1$). Thus, the CPC strength can be found directly from the modulation frequency that zeros the throughput modulation amplitude. In practice, minimizing that amplitude is sufficient, at least in the cases of CMIT and ATS, because even when the second numerator term is not zero, the first will be minimized at a value of Ω that is not very different from the $\Omega_{\min}$ of Eq. (10). Calculations using approximate parameter values and experimental results both lead to an estimated 10% uncertainty in determining $\Omega = \Omega_{\min}$.

The ring cavity model described above has been incorporated into a *Mathematica* program for calculation of the CMIT and CMIA behavior resulting from CPC. In the program, measured experimental parameter values are input, and the CPC strength is treated as an adjustable parameter. The program has previously been used to determine the CPC strength by fitting the experimental throughput spectrum, and to study slow and fast light in CMIT and CMIA by modulating the input with a Gaussian pulse [22]. In the results presented here, the input amplitude is sinusoidally modulated to predict the expected throughput modulation amplitude and phase shift. The modulation frequency that gives the minimum throughput modulation amplitude on resonance determines the CPC strength via Eq. (10).

To check the approximations made in Eq. (10) and in its derivation, we considered some experimentally realistic cases of CMIT and ATS in the model program described above when artificial T_c values were input [34]. For those test cases, the program was used to find the modulation frequency $\Omega_{\min}$ giving the minimum throughput modulation amplitude on resonance. In these examples, the square of $\Omega_{\min}$ depended linearly on T_c. This showed that our approximation in Eq. (10) is reasonable, at least for CMIT and ATS where the two Qs are very different. In general, Eq. (10) allows us to find T_c to within 20%, where part of the uncertainty is in the estimate of the effective refractive indices that appear in the round-trip times. Having thus established a proportional relation between $\Omega_{\min}^2$ and T_c, we can directly estimate the CPC strength experimentally by simply finding the modulation frequency corresponding to minimum modulation amplitude on resonance, without the need to fit the throughput spectrum to a computer model.

III. EXPERIMENTAL RESULTS

To determine the CPC strength in CMIT and ATS, we used an experimental setup [22] as shown in Fig. 2.

The tunable diode laser ($\lambda = 1508$–1580 nm) is scanned in frequency by a function generator (FG1). The free-space output beam from the laser head passes through an anamorphic prism (AP) and optical isolator (OI). An acousto-optic modulator (AOM), controlled by function generator FG2, is then used to amplitude-modulate the deflected beam. Before going to the fiber coupler (FC), the deflected light beam passes through a set of wave plates (WP) which are used to control the input polarization. Usually, the wave plates are adjusted to provide linearly polarized light incident on the microresonator. The fiber coupler FC launches the light into a single mode fiber. The fiber isolator is used to prevent interference due to backward propagating light. The single mode fiber is also mounted in a compression-based polarization controller (PC), for further regulation of the input polarization. The region of the fiber after the PC is tapered to a diameter of 2–3 μm for coupling to the microresonator and kept short and straight to preserve the polarization. The throughput light is collimated and sent to a polarization analyzer (PA), described below.

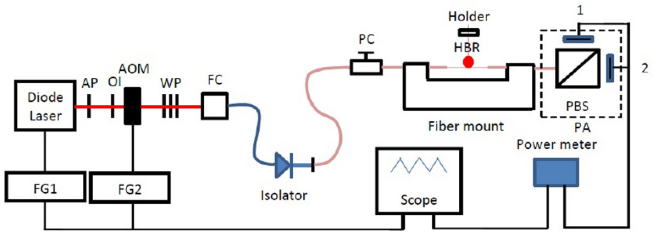

FIG. 2. Experimental setup for dynamical determination of the CPC strength in a single microresonator. This figure is reproduced from Ref. [22].

We use a hollow-bottle resonator (HBR) [35] in our experiments. Due to its bottle shape, the HBR has some advantages. Bottle resonators provide the benefits of high Q, tunability (by stretching), axial mode confinement, and mode selectivity (by axial positioning of the coupling fiber). A WGM in an HBR is described by three mode indices: The azimuthal index m is the number of wavelengths in the circumference, the radial index p is the number of radial intensity maxima, and the axial index q is the number of axial field nodes. The WGMs of an HBR can be tuned easily by stretching the resonator, and the two polarizations tune at different rates, so coresonance can be imposed, rather than having to achieve it by coincidence. To make the HBR, a fused-silica capillary is internally etched with a hydrofluoric acid–methanol solution to thin its walls to a thickness of 5–10 μm, and then a short length is heated using a hydrogen torch while under internal air pressure, leading to the formation of a bottle-shaped bulge [36]. A typical HBR used in our experiments is shown in Fig. 3.

The coupling region of the fiber is made adiabatically bitapered and brought into contact with the HBR in its equatorial plane (axial position of maximum diameter). The HBR is mounted on a piezo-controlled holder for strain tuning. In all cases, the resonator is kept inside an acrylic box to minimize temperature fluctuations and other effects of air movement. The collimated output light is sent to a polarization analyzer (PA) which includes the polarizing beam splitter (PBS) and two detectors, a fast detector (1) and a slow detector (2). The PA can be rotated about the fiber axis so that either detector can detect either polarization.

Adjustment of the input polarization to TE or TM and strain tuning to coresonance will result in the throughput power vs scanned laser frequency showing the spectral features of CMIT or ATS because of CPC. For either TE or TM input polarization, we need to observe the CMIT or ATS feature on the fast detector (1) to see the throughput response

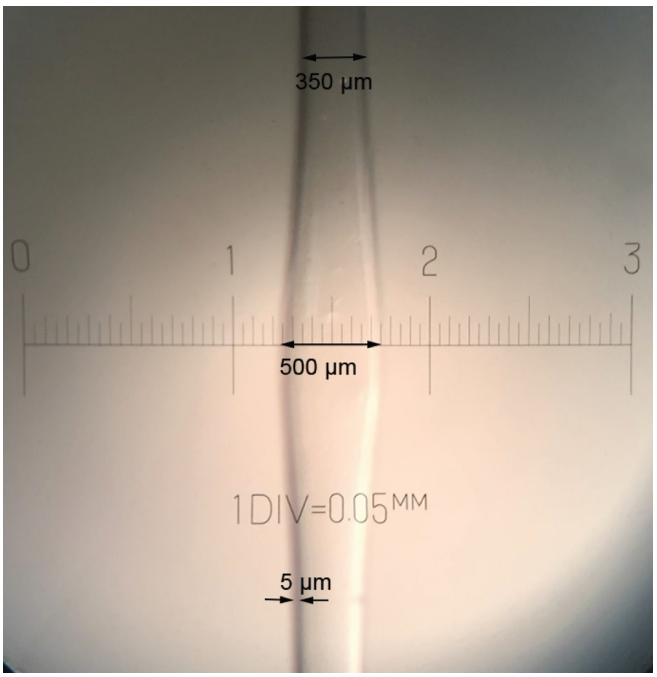

FIG. 3. A hollow-bottle resonator (HBR) obtained by manual compression of air inside the capillary. Initial diameter of the capillary is about 350 μm and the diameter at the bulge is about 500 μm. The wall thickness is about 5 μm after etching.

to the input amplitude modulation (Fig. 4). The modulation frequency of the AOM is in the range of a few MHz, and the slow detector cannot respond to these frequencies. So, in our experiments when we have TE input, we can observe the throughput response in the fast detector channel without rotating the analyzer. When we have TM input, we simply rotate the analyzer by 90 °.

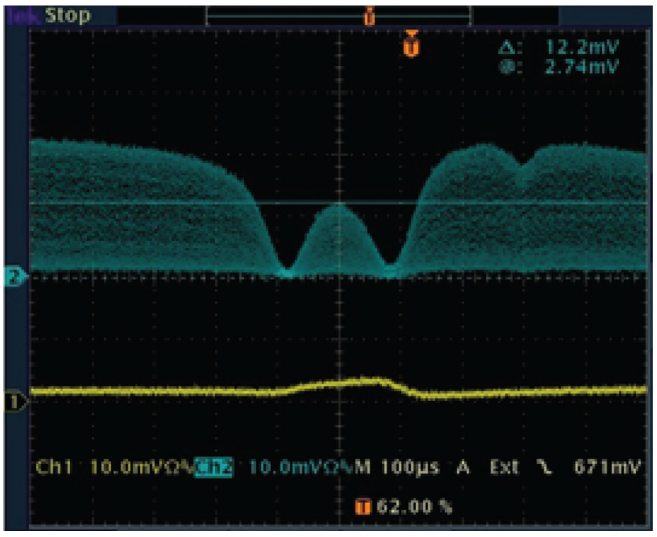

FIG. 4. Modulation response on the fast detector channel (upper, blue trace) and on the slow detector channel (lower, yellow trace) at a modulation frequency of 1 MHz. As we change the modulation frequency, there is an obvious minimum in the amplitude on resonance (at the central peak) in the fast detector response while the slow detector response (output polarization orthogonal to input) is unaffected.

During the experiment, CPC obscures the individual mode parameters of the coresonant TE and TM modes. Therefore, to determine the individual mode linewidths, quality factors, dip depths, and coupling regimes, detuning the modes from coresonance is necessary. To do this, as detailed in Ref. [22], the HBR is stretched axially for strain detuning. Then we can look at the individual modes in each polarization and measure their mode parameters. The orthogonally polarized modes are then brought back to coresonance, recovering the CMIT or ATS feature and confirming that it results from CPC. Further confirmation comes from the presence of some nonzero power in the orthogonal polarization throughput channel in Fig. 4, indicating that our CMIT or ATS effects are truly the result of cross coupling between the two polarizations rather than interference between modes of the same polarization. The individual mode parameters are then used to fit the model throughput spectrum to the experimental spectrum by adjusting the value of CPC strength in the model to get our first estimate of T_c [22]. Examples of numerical fitting of CMIT and ATS for estimating the value of T_c are shown in Figs. 5(a) and 6(a), respectively.

In each case, a second estimate of T_c is found by turning on the input modulation and finding the modulation frequency that gives the minimum throughput amplitude on resonance (at the central peak) relative to the input modulation amplitude (throughput, measured far off resonance). The relation in Eq. (10) gives that other estimate of T_c. Figures 5(b) and 6(b) show the relative modulation amplitude at the fitted T_c given by the model, as well as the observed minimum relative modulation amplitude in the experiment and the corresponding modulation frequency, which is used to calculate the second value of T_c. In the captions, detuning refers to the difference $\nu_2 - \nu_1$ of the resonant frequencies of the two WGMs—the frequency of the orthogonal WGM relative to the frequency of the driven WGM. The detunings are less than the width of the higher-Q WGM and do not affect the second method of finding T_c.

In Figs. 5(b) and 6(b), the experimentally observed minimum resonant throughput amplitude is indicated by the green dashed line. Since the simulated throughput modulation is based on the fitted T_c, if the simulated and experimental throughput modulation amplitudes agree, the value of the modulation-derived T_c should be nearly equal to the fitted T_c. The results of the two methods agree to within 2.5% in the case of Fig. 5, and to within 15.5% in the case of Fig. 6.

Since the AOM produces full amplitude modulation, the input essentially consists of just the two sidebands at $\pm\nu_{\min} = \pm\,\Omega_{\min}/2\pi$. This means that the throughput modulation amplitudes in Figs. 5(b) and 6(b) roughly match the throughput at the minima in Figs. 5(a) and 6(a), respectively, which are located at approximately $\pm\nu_{\min}$ relative to the central peak.

The finite response time of the AOM limits the modulation frequency to less than 10 MHz. This then restricts the range of cases of CMIT and ATS for which both methods of finding T_c can be applied.

The presence of mode overlap in the throughput spectra can make it difficult to find clear CMIT and ATS features. However, by using tapered fibers with different diameters and

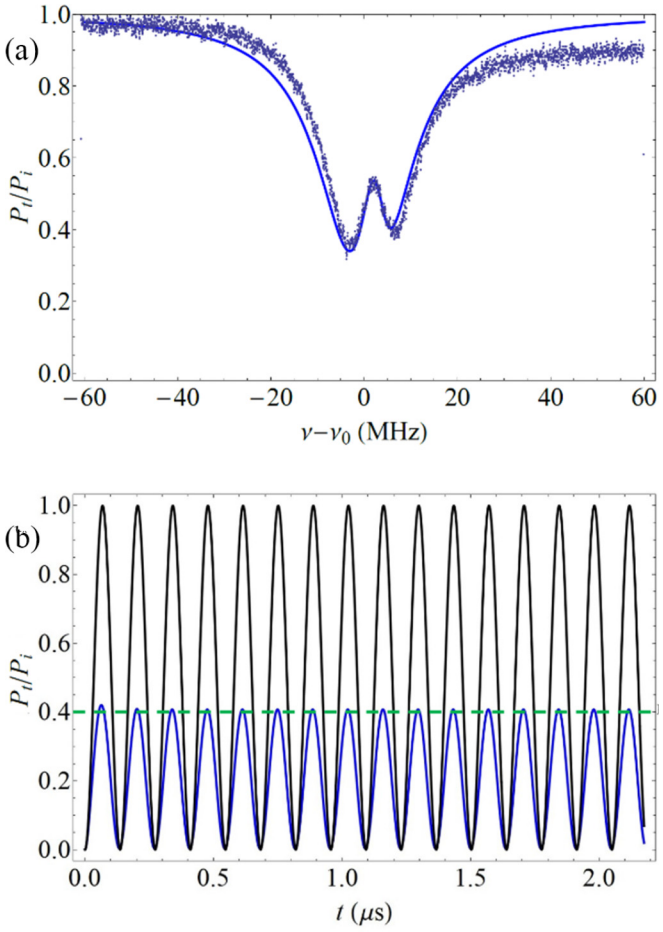

FIG. 5. CMIT (TE input) with 200-μm-radius HBR. (a) Model throughput spectrum (blue solid line) fit to the experimental throughput (gray trace), giving $T_c = 1.99 \times 10^{-8}$. This figure [panel (a)] is reproduced from Ref. [21]. (b) Model-predicted resonant throughput modulation (blue, amplitude of 0.40) relative to input modulation (gray, amplitude of 1.0), corresponding to the fitted T_c in (a). Mode parameters: $Q_1 = 9.6 \times 10^6$, $Q_2 = 5.2 \times 10^7$; $M_1 = 0.70$ (undercoupled), $M_2 = 0.65$ (undercoupled); detuning = 2.3 MHz. An experimental minimum relative modulation amplitude of 0.40 was found (green dashed line) at 4.0 MHz using the AOM, giving $T_c = 2.04 \times 10^{-8}$.

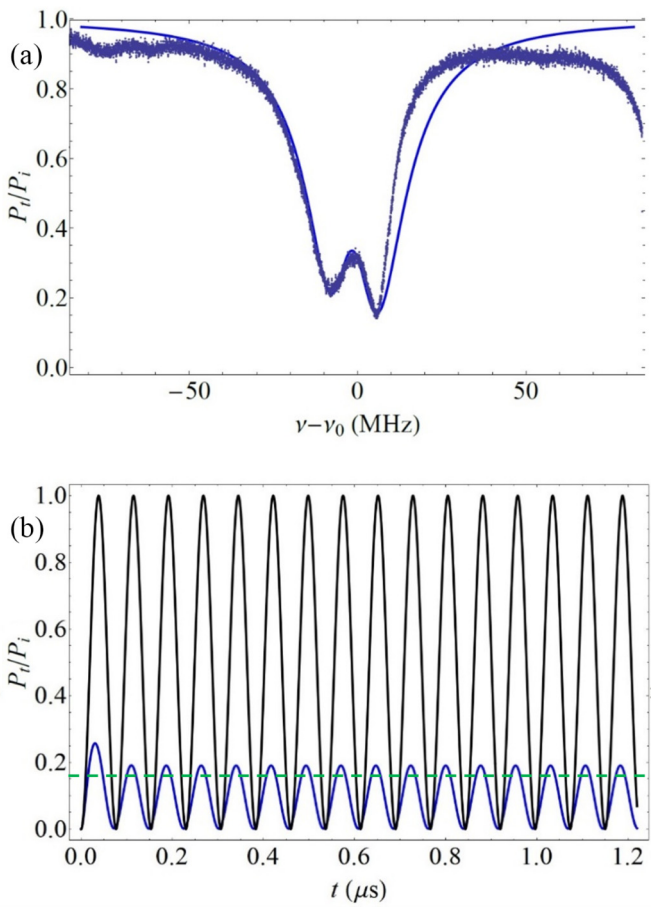

FIG. 6. ATS (TE input) with 180-μm-radius HBR. (a) Model throughput spectrum (blue solid line) fit to the experimental throughput (gray trace), giving $T_c = 3.98 \times 10^{-8}$. (b) Model-predicted resonant throughput modulation (blue, amplitude of 0.19) relative to input modulation (gray, amplitude of 1.0), corresponding to the fitted T_c in (a). Mode parameters: $Q_1 = 8.0 \times 10^6$, $Q_2 = 2.3 \times 10^7$; $M_1 = 0.93$ (undercoupled), $M_2 = 0.72$ (undercoupled); detuning = –2.0 MHz. An experimental minimum relative modulation amplitude of 0.15 was found (green dashed line) at 6.7 MHz using the AOM, giving $T_c = 4.65 \times 10^{-8}$.

positioning the fiber carefully near the HBR's equator (axial position of maximum diameter), it was possible to reduce the mode density and minimize mode overlap of the WGMs.

For twenty cases of CMIT and ATS, using four HBRs with different radii and different tapered fiber diameters (HBR radii 180, 190, 200, and 220 μm; tapered fiber diameters ranging from 2 to 3 μm), we estimated the CPC strength T_c (fit) from model fitting and found another estimate of CPC strength T_c (mod) from amplitude modulation. For each case, we use Eq. (7) to determine if it is CMIT or ATS. In Table I the values of T_c from numerical fitting and from amplitude modulation are compared; the modulation frequencies $\nu_{\min}$ range from 3.5 to 10.0 MHz. The first 15 cases have TE input, while the last five cases have TM input. The effective refractive indices of the two WGMs are assumed to be $n_1 = n_2 = 1.36$ [21].

The uncertainty in $\log_{10}(T_c)$ is ~0.1 in all the fitting done in the cases shown here, which means the T_c found by fitting has an uncertainty of 20%. The uncertainty in $\nu_{\min}$ is about 10%, as discussed earlier, so the uncertainty in the T_c found by modulation is also 20%. The percent difference is calculated as $[T_c(\text{mod}) - T_c(\text{fit})]/T_c(\text{average})$. Of the results, those with absolute percent difference less than 32% are within the expected experimental error; these comprise 14 out of 20 cases, consistent with 1σ uncertainty.

Comparison of the results of the two experimental methods of determining T_c is also shown graphically in Fig. 7. For each case in Table I, a point in T_c(fit)–T_c(mod) space is plotted, along with its error ellipse. A point lying on the solid 45 ° line would have $T_c(\text{mod}) = T_c(\text{fit})$. The two dashed lines represent the 32% expected experimental uncertainty limit noted above, and points between the dashed lines indicate agreement to within this limit. Another way to evaluate agreement is to note that points whose error ellipses intersect the solid 45 ° line

TABLE I. Comparing the values of T_c from numerical fitting and from amplitude modulation at $\nu_{\min} = \Omega_{\min}/2\pi$.

$\nu_{\min}$ (MHz)	Effect	Q_1, Q_2 ($\times 10^7$)	T_c (fit) ($\times 10^{-8}$)	T_c (mod) ($\times 10^{-8}$)	Diff. (%)
3.5	CMIT	1.5, 8.6 10	1.26	1.88	39.6
4.0	CMIT	0.96, 5.2	1.99	2.04	2.5
4.0	CMIT	1.6, 9.7	2.51	2.04	–20.7
4.5	CMIT	0.77, 3.7	1.58	2.10	28.3
5.0	CMIT	0.41, 5.0	2.51	2.59	3.1
6.5	CMIT	0.64, 6.4	3.98	4.86	19.9
6.5	CMIT	0.77, 5.4	1.26	4.36	110
4.1	ATS	0.19, 5.3	1.00	1.74	54
4.2	ATS	2.3, 2.9	1.99	1.82	–8.9
5.2	ATS	1.3, 2.7	3.16	2.79	–12.4
6.7	ATS	0.80, 2.3	3.98	4.65	15.5
7.2	ATS	0.85, 1.4	6.31	5.97	–5.5
8.5	ATS	0.58, 3.7	10.0	8.32	–18.3
9.0	ATS	1.3, 1.4	12.6	8.39	–40.5
9.5	ATS	0.50, 1.6	10.0	11.5	14.0
4.8	CMIT	0.75, 5.3	1.26	2.38	61.5
6.1	ATS	0.76, 2.7	3.16	3.84	19.4
7.5	ATS	0.70, 2.7	6.31	7.20	13.2
9.5	ATS	0.94, 2.0	6.31	9.37	39.0
10.0	ATS	0.45, 1.1	12.6	11.5	–9.1

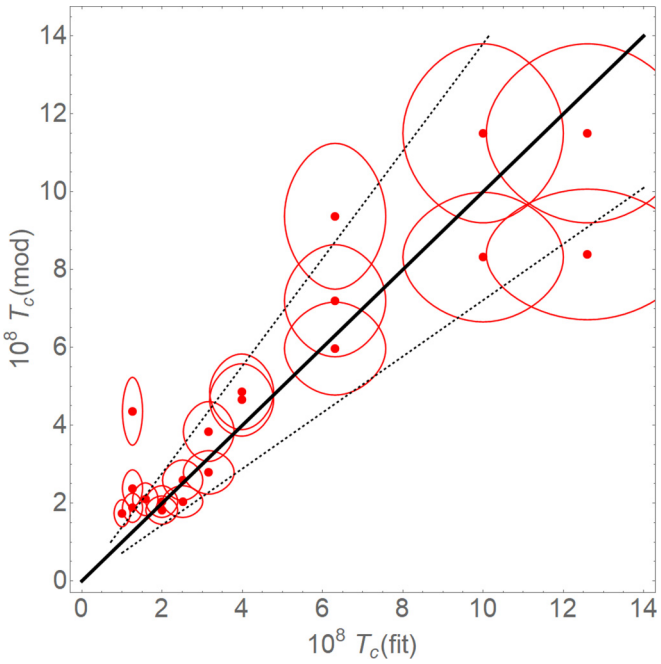

FIG. 7. Comparison of two methods of measuring T_c; data from Table I. If the two methods gave exactly the same value, the point for each case would fall on the solid line. A point lying between the dashed lines indicates agreement of the two methods to within experimental uncertainty. Agreement is also indicated by the intersection of a point's error ellipse with the solid line.

are also within experimental uncertainty. From Fig. 7, we see again that 14 out of 20 cases agree within experimental error.

Comparison between experiment and theory would require knowledge of the mode numbers m, p, and q for both WGMs. The estimated range of possible values of p and q [21] would lead to an uncertainty in T_c (theory) of nearly plus or minus two orders of magnitude. The experimental values are significantly more precise.

It can be seen from Table I and Fig. 7 that a positive percent difference is about twice as likely as a negative one. This can be understood from Eqs. (9) and (10). In the usual case of mode 1 being undercoupled, the expression in the second set of parentheses of the numerator of Eq. (9) will be positive; as a result, minimizing the first term in the numerator gives a minimum frequency somewhat larger than the expression in Eq. (10), slightly overestimating the value of T_c (mod). Only if mode 1 is overcoupled, or if the two Q values are not very different, will T_c(mod) be less than T_c(fit).

IV. CONCLUSIONS

Based on our results, we can say that we have developed an independent method of estimating the CPC strength, using input amplitude modulation, without the need to fit a numerical simulation to the experimental results. So far, we have three different methods for finding the CPC strength: a theoretical calculation, based on the transverse structure of WGMs of known mode numbers [21], and two experimental estimates, first by fitting a computational model to the experimental throughput spectrum to infer the CPC strength indirectly as in Ref. [22], and second by directly estimating the CPC strength from the response of the throughput amplitude to a sinusoidal modulation, as presented here. All three methods give the same range of orders of magnitude of the CPC strength, and the two experimental methods agree with each other, without requiring knowledge of the mode numbers of the WGMs.

Here, for the cases of CMIT and ATS, most of our results show reasonable agreement between the two experimental methods for determining the CPC strength. For the cases differing by more than the expected error, there might be several explanations. First, the CMIT feature itself can be hard to observe cleanly given the possibility of mode overlap in our experiment, and this can also lead to misidentification of the modes involved when they are detuned from coresonance. Second, our measurements of the individual mode parameters may not be completely accurate in every case; for example, it can be difficult to determine the coupling regime for a WGM with a deep throughput dip.

In addition to the potential experimental difficulties noted above, two assumptions made in our theoretical analysis may be violated in some cases. We assumed $Q_2 \gg Q_1$, but in five of the examples of Table I, the ratio of quality factors is about 2 or less, and the value found for T_c(mod) may be less than T_c(fit) since then κ_2^2 cannot be neglected in Eq. (10). Also, the second term in the numerator of Eq. (9) will usually not be zero, as assumed; this can lead to T_c(mod) being greater than or less than T_c(fit) for mode 1 undercoupled or overcoupled, respectively, as noted in the previous section.

Based on our previous work [21], the theoretical model used here allows for CPC from mode 1 to mode 2 to have a different strength than CPC from mode 2 to mode 1. This can be confirmed experimentally by observing the output polarized orthogonally to the input. We are currently pursuing

further CMIT and ATS experiments to test this feature of the model and to determine the two CPC strengths separately. This coupling nonreciprocity can make the properties of the exceptional point more interesting [32,33].

Other experimental goals are to further reduce mode overlap, to find more cases with $Q_2 \gg Q_1$, and to replace the AOM with a faster modulator, expanding the range of cases in which the two experimental methods can be compared. The results from further experiments will be analyzed to predict which parameter ranges should enhance experimental observation of the CPC effects.

The coupling effect between orthogonally polarized modes in a single resonator can lead to CMIT, CMIA, or ATS. These effects enable slow light or fast light and have other potential applications. Being able to determine the intermode coupling strength without model fitting will help us to get a better understanding of the dynamics of the CPC effect in microresonators. A good method for locating the exceptional point may enhance sensor applications of microresonators. For example, the analysis presented here also applies in the case of coupled resonators, if the coupling between resonators is not too strong. That coupling can be adjusted by varying the gap between the resonators, and so the system can be set at the exceptional point to take advantage of the enhanced sensitivity. We also expect other applications to be improved with the help of our dynamical study.

ACKNOWLEDGMENTS

We would like to thank Razvan I. Stoian, for developing the HBR fabrication procedures; Khoa V. Bui, for preparing the experimental setup; and Karleyda Sandoval, for setting up a PYTHON model for data analysis.

[1] M. R. Foreman, J. D. Swaim, and F. Vollmer, Whispering gallery mode sensors, Adv. Opt. Photonics **7**, 168 (2015).

[2] W. Yoshiki, Y. Honda, T. Tetsumoto, K. Furusawa, N. Sekine, and T. Tanabe, All-optical tunable buffering with coupled ultra-high Q whispering gallery mode microcavities, Sci. Rep. **7**, 10688 (2017).

[3] D. D. Smith, H. Chang, K. Myneni, and A. T. Rosenberger, Fast-light enhancement of an optical cavity by polarization mode coupling, Phys. Rev. A **89**, 053804 (2014).

[4] D. D. Smith, H. Chang, K. A. Fuller, A. T. Rosenberger, and R. W. Boyd, Coupled resonator induced transparency, Phys. Rev. A **69**, 063804 (2004).

[5] A. Naweed, G. Farca, S. I. Shopova, and A. T. Rosenberger, Induced transparency and absorption in coupled whispering-gallery microresonators, Phys. Rev. A **71**, 043804 (2005).

[6] L. Maleki, A. B. Matsko, A. A. Savchenkov, and V. S. Ilchenko, Tunable delay line with interacting whispering-gallery-mode resonators, Opt. Lett. **29**, 626 (2004).

[7] Q. Xu, S. Sandhu, M. L. Povinelli, J. Shakya, S. Fan, and M. Lipson, Experimental Realization of an On-Chip All-Optical Analogue to Electromagnetically Induced Transparency, Phys. Rev. Lett. **96**, 123901 (2006).

[8] X. Yang, M. Yu, D. L. Kwong, and C. W. Wong, All-Optical Analog to Electromagnetically Induced Transparency in Multiple Coupled Photonic Crystal Cavities, Phys. Rev. Lett. **102**, 173902 (2009).

[9] X. Zhou, L. Zhang, W. Pang, H. Zhang, Q. Yang, and D. Zhang, Phase characteristics of an electromagnetically induced transparency analogue in coupled resonant systems, New J. Phys. **15**, 103033 (2013).

[10] Y. F. Xiao, L. He, J. Zhu, and L. Yang, Electromagnetically induced transparency-like effect in a single polydimethylsiloxane-coated silica microtoroid, Appl. Phys. Lett. **94**, 231115 (2009).

[11] B. B. Li, Y. F. Xiao, C. L. Zou, Y. C. Liu, X. F. Jiang, Y. L. Chen, Y. Li, and Q. Gong, Experimental observation of Fano resonance in a single whispering-gallery microresonator, Appl. Phys. Lett. **98**, 021116 (2011).

[12] Y.-C. Liu, B.-B. Li, and Y.-F. Xiao, Electromagnetically induced transparency in optical microcavities, Nanophotonics **6**, 789 (2017).

[13] C. H. Dong, C.-L. Zou, Y.-F. Xiao, J.-M. Cui, Z.-F. Han, and G.-C. Guo, Modified transmission spectrum induced by two-mode interference in a single silica microsphere, J. Phys. B: At., Mol. Opt. Phys. **42**, 215401 (2009).

[14] Q. Huang, Z. Shu, G. Song, J. Chen, J. Xia, and J. Yu, Electromagnetically induced transparency-like effect in a two-bus waveguides coupled microdisk resonator, Opt. Express **22**, 3219 (2014).

[15] Y. Yang, S. Saurabh, J. Ward, and S. Nic Chormaic, Coupled-mode-induced transparency in aerostatically tuned microbubble whispering-gallery resonators, Opt. Lett. **40**, 1834 (2015).

[16] S. Ramelow, A. Farsi, S. Clemmen, J. S. Levy, A. R. Johnson, Y. Okawachi, M. R. E. Lamont, M. Lipson, and A. L. Gaeta, Strong polarization mode coupling in microresonators, Opt. Lett. **39**, 5134 (2014).

[17] Y. Wang, K. Zhang, S. Zhou, Y.-H. Wu, M.-B. Chi, and P. Hao, Coupled-mode induced transparency in a bottle whispering-gallery-mode resonator, Opt. Lett. **41**, 1825 (2016).

[18] Y. Zheng, J. Yang, Z. Shen, J. Cao, X. Chen, X. Liang, and W. Wan, Optically induced transparency in a micro-cavity, Light: Sci. Appl. **5**, e16072 (2016).

[19] D. V. Strekalov, R. J. Thompson, L. M. Baumgartel, I. S. Grudinin, and N. Yu, Temperature measurement and stabilization in a birefringent whispering gallery mode resonator, Opt. Express **19**, 14495 (2011).

[20] K. Ma, Y. Zhang, H. Su, G. Yi, C. Yu, and J. Wang, Autler-Townes splitting and induced transparency windows in a multimode microfiber knot, Opt. Lett. **45**, 754 (2020).

[21] A. T. Rosenberger, E. B. Dale, K. V. Bui, E. K. Gonzales, D. Ganta, L. Ke, and S. R. Rajagopal, Cross-polarization coupling of whispering-gallery modes due to the spin-orbit interaction of light, Opt. Lett. **44**, 4163 (2019).

[22] K. V. Bui and A. T. Rosenberger, Coupled-mode-induced transparency and attenuation resulting from cross-polarization coupling, Phys. Rev. A **101**, 033836 (2020).

[23] G. Guan and F. Vollmer, Polarized transmission spectra of the fiber-microsphere system, Appl. Phys. Lett. **86**, 121115 (2005).

[24] H. Konishi, H. Fujiwara, S. Takeuchi, and K. Sasaki, Polarization-discriminated spectra of a fiber-microsphere system, Appl. Phys. Lett. **89**, 121107 (2006).

[25] P. Bianucci, C. R. Fietz, J. W. Robertson, G. Shvets, and C.-K. Shih, Polarization conversion in a silica microsphere, Opt. Express **15**, 7000 (2007).

[26] P. Bianucci, C. R. Fietz, J. W. Robertson, G. Shvets, and C.-K. Shih, Whispering gallery mode microresonators as polarization converters, Opt. Lett. **32**, 2224 (2007).

[27] M. N. M. Nasir, S. B. Gorajoobi, G. S. Murugan, and M. N. Zervas, Polarization effects in optical microresonators, J. Opt. Soc. Am. B **36**, 705 (2019).

[28] F. Lei, J. M. Ward, P. Romagnoli, and S. Nic Chormaic, Polarization-Controlled Cavity Input-Output Relations, Phys. Rev. Lett. **124**, 103902 (2020).

[29] J. Kreismann and M. Hentschel, Spin-orbit interaction of light in three-dimensional microcavities, Phys. Rev. A **102**, 043524 (2020).

[30] C. Wang, X. Jiang, W. R. Sweeney, C. W. Hsu, Y. Liu, G. Zhao, B. Peng, M. Zhang, L. Jiang, A. D. Stone, and L. Yang, Induced transparency by interference or polarization, Proc. Natl. Acad. Sci. USA **118**, e2012982118 (2021).

[31] B. Peng, S. K. Ozdemir, W. Chen, F. Nori, and L. Yang, What is and what is not electromagnetically induced transparency in whispering-gallery microcavities, Nat. Commun. **5**, 5082 (2014).

[32] M.-A. Miri and A. Alù, Exceptional points in optics and photonics, Science **363**, eaar7709 (2019).

[33] J. Wiersig, Review of exceptional point-based sensors, Photonics Res. **8**, 1457 (2020).

[34] L. Ke, S. R. Rajagopal, and A. T. Rosenberger, Numerical and experimental study of the dynamics of cross polarization coupling in a single whispering-gallery microresonator, Proc. SPIE **10904**, 109041T (2019).

[35] G. S. Murugan, M. N. Petrovich, Y. Jung, J. S. Wilkinson, and M. N. Zervas, Hollow-bottle optical microresonators, Opt. Express **19**, 20773 (2011).

[36] R.-I. Stoian, K. V. Bui, and A. T. Rosenberger, Silica hollow bottle resonators for use as whispering gallery mode based chemical sensors, J. Opt. **17**, 125011 (2015).